Materials Advances

ROYAL SOCIETY OF CHEMISTRY

PAPER

View Article Online
View Journal | View Issue

Cite this: *Mater. Adv.*, 2023, 4, 3853

A SBA-15-templated mesoporous $NiFe_2O_4$/MXene nanocomposite for the alkaline hydrogen evolution reaction†

Munawar Khalil, *[ab] Michael Lesa,[ab] Alexander G. Juandito,[bc] Afiten R. Sanjaya,[a] Tribidasari A. Ivandini,[a] Grandprix T. M. Kadja,[def] Muhammad Haris Mahyuddin,[eg] Mehran Sookhakian[hi] and Yatimah Alias[hi]

The development of efficient and cost-effective electrocatalysts for the hydrogen evolution reaction (HER) is crucial for renewable energy conversion and storage. Here, we report the synthesis of a mesoporous $NiFe_2O_4$/MXene nanocomposite for the alkaline HER. The as-prepared nanocomposite demonstrated a synergistic effect in facilitating the HER, as evidenced by significantly improved electrocatalytic activity compared to individual $NiFe_2O_4$ and MXene components. The mesoporous structure of the nanocomposite, derived from the SBA-15 template, provided a large surface area and enhanced mass transport, while the incorporation of MXene as a conductive additive improved the charge transfer kinetics. Based on the results, the $NiFe_2O_4$/MXene nanocomposite exhibited a low onset overpotential of −440 mV, a small Tafel slope of 187.5 mV per decade, and long-term stability for the HER in alkaline electrolytes, as opposed to the individual $NiFe_2O_4$ or MXene. The enhanced electrocatalytic performance was attributed to the synergistic effect of the unique mesoporous structure, high conductivity, and abundant active sites provided by $NiFe_2O_4$ and MXene. However, DFT calculations revealed that more favorable H atom adsorption and activation processes were observed on the surface of the $NiFe_2O_4$ (400) plane. Our findings highlight the potential of using templated mesoporous nanocomposites for designing efficient electrocatalysts for the alkaline HER and contribute to the advancement of renewable energy technologies.

Received 10th June 2023,
Accepted 1st August 2023

DOI: 10.1039/d3ma00289f

rsc.li/materials-advances

Introduction

Replacing fossil fuel-based energy resources with renewable ones has been one of the main agendas for developing clean and sustainable energy.[1,2] Nevertheless, many current renewable energy resources, such as solar, wind, or geothermal, are known to be temporal and spatially intermittent, which could potentially lead to low energy delivery and hamper their daily applications.[3–5] Therefore, conversion of such renewable energy resources into storable and transferable chemical fuels is desired.[6,7] Among different candidates for such chemical fuels, hydrogen gas has attracted much attention as a clean fuel due to its high energy density (283 kJ mol^{-1}) and because it produces zero emission during consumption.[8] Currently, hydrogen gas is mainly made from industrial steam reforming. However, the high cost, low conversion efficiency, and carbon dioxide production (a major contributor to global warming) as a by-product make such a process undesirable for clean, economical, and sustainable hydrogen production.[9] Recently, electrochemical water splitting has been considered one of the most promising pathways for producing clean and sustainable hydrogen gas.[10–12] In general,

[a] *Department of Chemistry, Faculty of Mathematics and Natural Sciences, Universitas Indonesia, 16424, Depok, West Java, Indonesia. E-mail: mkhalil@sci.ui.ac.id*
[b] *Low Dimension Materials Lab, Department of Chemistry, Faculty of Mathematics and Natural Sciences, Universitas Indonesia, 16424, Depok, West Java, Indonesia*
[c] *Department of Physics, Faculty of Mathematics and Natural Sciences, Universitas Indonesia, 16424, Depok, West Java, Indonesia*
[d] *Division of Inorganic and Physical Chemistry, Institut Teknologi Bandung, Jalan Ganesha No. 10, Bandung, 40132, Indonesia*
[e] *Research Center for Nanosciences and Nanotechnology, Institut Teknologi Bandung, Jalan Ganesha No. 10, Bandung, 40132, Indonesia*
[f] *Center for Catalysis and Reaction Engineering, Institut Teknologi Bandung, Jalan Ganesha No. 10, Bandung, 40132, Indonesia*
[g] *Research Group of Advanced Functional Materials, Faculty of Industrial Technology, Institut Teknologi Bandung, Jalan Ganesha No. 10, Bandung, 40132, Indonesia*
[h] *Department of Chemistry, Faculty of Science, Universiti Malaya, 50603, Kuala Lumpur, Malaysia*
[i] *Universiti Malaya Centre for Ionic Liquids (UMCiL), Universiti Malaya, 50603, Kuala Lumpur, Malaysia*

† Electronic supplementary information (ESI) available. See DOI: https://doi.org/10.1039/d3ma00289f

electrochemical water splitting proceeds in two significant concerted reactions occurring at both the cathode and anode. The reaction at the cathode is known as the hydrogen evolution reaction (HER), while the reaction at the anode is commonly known as the oxygen evolution reaction (OER). In a typical alkaline-based electrolyte, the HER occurs *via* the Volmer–Tafel or Volmer–Heyrovsky mechanism depending on the type of electrocatalyst.[13,14] Nevertheless, the application of such a process for large-scale hydrogen gas production is still hampered by the high HER overpotential, making the overall reaction kinetics very slow. One way to solve this shortcoming is by developing an efficient and highly active electrocatalyst to facilitate fast and efficient HER.[15] Traditionally, platinum (Pt) metal has been the most effective electrocatalyst in the HER due to its ability to generate a small onset potential and low overpotential. However, the utilization of such a low abundant and expensive rare earth metal-based catalyst is less preferred in developing an affordable hydrogen production economy. Therefore, the fabrication of effective and highly active HER electrocatalysts from low-cost earth-abundant elements is highly needed.

In the literature, non-noble transition metal oxides, especially spinel ferrites like $NiFe_2O_4$, have gained great attention as emerging electrocatalysts for water electrolysis due to their large natural abundance, environmental friendliness, and cheapness.[16–19] For instance, Chanda *et al.* reported $NiFe_2O_4$ exhibited promising catalytic activity and durability as an electrocatalyst for the HER under alkaline conditions using different types of polymer binders.[16] Based on the results, it was revealed that the electrocatalyst was able to generate a considerably high current density of 125 mA cm^{-2} at 1.85 V using MEA containing qPPO as the polymer binder. In another report, Nivetha and co-workers successfully prepared $NiFe_2O_4$/graphene nanocomposites and applied them for the HER in 0.5 M H_2SO_4 solution.[20] Here, electrochemical measurements revealed that the nanocomposites exhibited a low overpotential of 259 mV and a Tafel slope of 121.4 mV dec^{-1}. Furthermore, Mukherjee and co-workers also revealed that a uniformly decorated reduced graphene oxide (RGO) sheet with $NiFe_2O_4$ nanoparticles with an average size of ~10.5 nm was found to be effective as an efficient electrocatalyst for the HER in acidic medium with a low onset overpotential of 5 mV *vs.* RHE with high cathodic current density and a low Tafel slope of 58 mV dec^{-1}.[21] Additionally, recent studies have also reported that many physicochemical properties of many transition metal oxides could easily be fine-tuned making them possess porous properties. During the past several years, nanocasting using mesoporous silica as a hard template was regarded as the most common method for fabrication of porous metal oxide nanoparticles.[22] For example, our recent study revealed that nanocasting using two different mesoporous silicas (KCC-1 and MCM-41) resulted in porous NiO nanoparticles with different physicochemical behaviors and catalytic activity against the reduction of *p*-nitrophenol.[23] Based on the results, porous NiO nanoparticles prepared with MCM-41 showed greater catalytic activity due to their larger surface area and better molecular diffusion. Recently, Kamali-Heidari and co-worker also reported that nanocasting of porous $NiFe_2O_4$ using SBA-15 was able to significantly increase its surface area to 198 m^2 g^{-1} and improve its performance as a reliable anode material for lithium ion batteries.[24]

Another emerging material that recently received great attention for a HER electrocatalyst is a two-dimensional material known as MXene.[25] Typically, MXene has a chemical composition of $M_{n+1}X_nT_x$, where carbon-based MXene, *i.e.*, $Ti_3C_2T_x$ is the most commonly known MXene. MXene reportedly has a high absorption capacity and a high hydrophilicity value.[26,27] Additionally, it is also reported that MXene could also facilitate charge transfer due to its high metallic conductivity.[28,29] Therefore, MXene has recently emerged as one of the good candidates for electrocatalysts for HER reactions. For example, Zhang and co-workers found that a Pt-deposited MXene electrocatalyst had a better catalytic performance than pure platinum.[30] Based on the results, Pt-deposited Mxene, which was prepared using atomic layer deposition (ALD), exhibited a low overpotential of 67.8 mV at a relatively low Pt content (1.7 wt%). Recently, a study reported by Lv *et al.* also revealed that synergistic combination of Mxene and Ni_2P supported by 3D Ni foam was able to enhance hydrophobicity, conductivity, and catalytic activity of the electrocatalyst for the HER in alkaline medium.[31] In this work, the Ni_2P/Mxene/NF composite exhibited a low overpotential of 135 mV at a current density of 10 mA cm^{-2} and showed excellent durability in 1 M KOH as the electrolyte. Motivated by the great potential, this work therefore aims to study the application of the mesoporous $NiFe_2O_4$/Mxene composite as an electrocatalyst for the HER in alkaline medium. Here, mesoporous $NiFe_2O_4$ (*m*-$NiFe_2O_4$) nanoparticles were prepared *via* a nanocasting approach where mesoporous silica SBA-15 was used as the hard template. Meanwhile, Mxene was synthesized *via* an etching and exfoliation technique. Here, the as-prepared composite was deposited on a glassy carbon electrode (GCE) as an electrode substrate where its catalytic activity for the HER was electrochemically evaluated in 1 M NaOH.

Experimental methods

Materials

Poly(ethylene glycol)-*block*-poly(propylene glycol)-*block*-poly(ethylene glycol) (Pluronic® P-123, PEG-PPG-PEG) (average M_n ~ 5800), hydrochloric acid (HCl, 37% wt in H_2O, purity: 99.99%), and tetraethyl *ortho*-silicate (TEOS) (purity: 99.0%) were purchased from Sigma-Aldrich and used in the synthesis of SBA-15. Meanwhile, nickel(II) nitrate hexahydrate ($Ni(NO_3)_2{\cdot}6H_2O$) (purity: 97%), iron(III) nitrate nonahydrate ($Fe(NO_3)_3{\cdot}9H_2O$) (purity: 97%), ethanol (C_2H_5OH) (purity: 99.5%), and sodium hydroxide (NaOH) (purity: 99.5%) from Sigma-Aldrich were used for fabricating *m*-$NiFe_2O_4$ nanoparticles. Furthermore, MAX phase ceramic carbon titanium aluminium carbon (Ti_3AlC_2) ~ 325 mesh (purity: 98%) was purchased from Advanced Materials Development Expert Store, China, while lithium fluoride (LiF) (powder, ~300 mesh) and dimethyl sulfoxide (DMSO) (purity: 99.9%) from Sigma-Aldrich were used in the synthesis of

MXene. Finally, Nafion™ 177 containing solution (~5% in a mixture of lower aliphatic alcohols and water) was purchased from Sigma-Aldrich and used in the fabrication of electrodes.

Synthesis of SBA-15

In this study, mesoporous silica SBA-15 was used as the hard template and was synthesized using a method reported by Zhou and co-workers with slight modifications.[32] Typically, 4 g of Pluronic P-123 was dissolved in an acid solution containing 19.5 mL of 37% HCl and 127 mL of deionized water. Afterwards, the solution was stirred using a magnetic stirrer for 3 hours in a water bath at a temperature of 40 °C at 500 rpm. Subsequently, 8.52 g of TEOS was added and the mixture was then transferred to a 250 mL polypropylene (PP) bottle, while heating at 90 °C for 24 hours. After the reaction, the solution was filtered using a Buchner filter followed by washing with water and ethanol successively. The resulting precipitate was dried in an oven for 24 hours at a temperature of 70 °C. Finally, the final SBA-15 can be obtained by calcining the powder at a temperature of 500 °C for 5 hours at a heating rate of 1.5 °C min^{-1}.

Synthesis of mesoporous $NiFe_2O_4$ (*m*-$NiFe_2O_4$)

Nanocasting method using the as-prepared SBA-15 was used to prepare *m*-$NiFe_2O_4$. Here, 0.2 g of $Ni(NO_3)_2{\cdot}6H_2O$ and 0.55 g of $Fe(NO_3)_3{\cdot}9H_2O$ were dissolved in 5 ml of ethanol. Then, 0.5 g of SBA-15 was then added to the solution and stirred for 12 h. The solution was then dried for 12 hours at 60 °C. The resulting powder was calcined at 250 °C for 4 hours at a heating rate of 1 °C min^{-1}, followed by second calcination at 600 °C for 5 hours at a heating rate of 1 °C min^{-1}. Subsequently, the mesoporous silica template was then etched away by dissolving the powder in a 2 M NaOH solution at 40 °C and stirred for 24 h. Finally, the final mesoporous $NiFe_2O_4$ was collected by centrifugation at 10 000 rpm, followed by drying in a vacuum oven overnight.

Synthesis of MXene

In this work, the synthesis of MXene was carried out using an etching and exfoliation method. In this method, 15 mL of 9 M HCl solution was initially mixed with 1.5 g of LiF in a 250 mL PP bottle while vigorously stirring for 30 min. Afterwards, 1.5 g of Ti_3AlC_2 was gradually added to the mixture and further stirred for another 24 hours at 50 °C. Next, the mixture was centrifuged for 5 minutes at 3500 rpm. The precipitate was then collected and washed with distilled water until the pH of the water reached 5–6 followed by drying in a vacuum oven at 60 °C. Subsequently, 0.3 g of the precipitate was then redispersed in 5 mL of DMSO and stirred for another 24 hours. The mixture was then centrifuged for 30 min at 3500 rpm and the precipitate was redispersed in 150 mL of distilled water and ultrasonicated for 10 h. The mixture was then centrifuged again at 3500 rpm for 5 min. Finally, the supernatant was collected and freeze-dried to obtain the final MXene product.

Preparation of *m*-$NiFe_2O_4$/MXene nanocomposite

Here, a nanocomposite of the as-prepared *m*-$NiFe_2O_4$ and MXene was prepared using a hydrothermal method. Typically, 40 mg of MXene was dispersed in 20 mL of distilled water and ultrasonicated for 30 min. In a separate container, 80 mg of porous $NiFe_2O_4$ nanoparticles was dispersed in 20 mL of distilled water and ultrasonicated for 30 min. Subsequently, the two solutions were then mixed and stirred using a magnetic stirrer for 40 min and transferred to a 100 mL Teflon-lined stainless-steel autoclave followed by heating at 100 °C for 4 h. Finally, the precipitate was then collected using centrifugation and dried overnight at 60 °C.

Characterization

Several characterization methods were employed to evaluate the physicochemical properties of the as-prepared nanoparticles and nanocomposites. In this work, crystallographic analysis was performed using a PANanalytical X'Pert Pro MPD (PANanalytical B.V., Amelo, the Netherlands), where Cu-Kα was used as the source. Meanwhile, Raman spectroscopic analysis was performed using a Horiba LabRAM HR Evolution equipped with a 523 nm laser source. To investigate the structural and morphological features of the samples, micrographic and selected area electron diffraction (SAED) analyses were performed using a high-resolution transmission electron microscope (HRTEM, TECNAI G2 Spirit Twin), while the structural images of the sample were also observed using a scanning electron microscope (SEM, ThermoFisher Scientific Axia ChemiSEM). Finally, the surface properties of the samples were also analyzed using a Quantachrome Quadrasorb Evo Surface Area and Pore Size Analyzer.

Electrode preparation

In this study, a glassy carbon electrode (GCE) was used as the electrode substrate, and was freshly polished prior to the application of electrocatalysts *via* a drop-casting method. Typically, 5 mg of each electrocatalyst, *i.e.*, *m*-$NiFe_2O_4$, MXene, and *m*-$NiFe_2O_4$/MXene, was dispersed in 1 mL of DI water, while ultrasonicated for 30 min. Afterwards, 30 μL of the electrocatalyst colloidal solution was further mixed with 1 μL of Nafion solution. Finally, 10 μL of the mixture was drop cast onto the surface of GCE and let dry at room temperature.

Electrochemical measurements

To evaluate the performance of the electrocatalysts, several electrochemical measurements were carried out using a three-electrode system potentiostat (ED410 e-corder, eDAQ). Herein, a Pt-wire and Ag/AgCl were used as counter and reference electrodes, respectively. Meanwhile, both bare and modified GCE were used as working electrodes in 1 M NaOH as the electrolyte. To evaluate the performance of each electrocatalyst in the HER, linear sweep voltammetry (LSV) was carried out within the cathodic potential range of −0.6 to 2.0 V *vs.* Ag/AgCl with a scan rate of 5 mV s^{-1} to obtain the Tafel polarization curve. Here, Tafel analysis was carried out by fitting the experimental data to the Tafel equation ($\eta = b\log j + a$), where η is the overpotential, j represents the current density, and a is a constant. Electrochemical impedance spectroscopy (EIS) analysis was also carried out within a frequency range of 10^5–10^{-2} Hz. Moreover, stability tests were also conducted by performing both

chronoamperometry at 10 mA cm^{-1} for 9000 seconds and cyclic voltammetry at a scan rate of 100 mV s^{-1} for 1000 cycles in the non-faradaic region. Here, all potentials are reported *versus* RHE by converting the measured potentials using the following equation:

$$E_{RHE} = E_{Ag/AgCl} + 0.059pH + E^{\circ}_{Ag/AgCl} \quad (1)$$

where, E_{RHE} is the converted potential *vs.* RHE, $E_{Ag/AgCl}$ is the measured potential *vs.* Ag/AgCl, and $E^{\circ}_{Ag/AgCl}$ represents the standard potential at 25 °C (0.1976).

Theoretical calculations

DFT calculations were performed under the Kohn–Sham formulation as implemented in the Vienna *ab initio* simulation package (VASP).[33–36] The projector augmented wave (PAW) method was employed to describe the interaction between ion cores and electrons.[37,38] The electron exchange correlation was treated using the generalized gradient approximation (GGA) based on the Perdew–Burke–Ernzerhof (PBE) functional.[39] The plane wave basis sets with a cut-off energy of 550 eV were used for all calculations. To treat the strong correlation effects in $NiFe_2O_4$, a rotationally invariant GGA + U approach introduced by Dudarev *et al.* was used with effective Hubbard parameters (U_{eff}) being 3.90 and 6.40 eV, respectively, for the Fe and Ni 3d orbitals, as suggested by Wang and co-workers.[40,41] The semiempirical Grimme's D3 method was employed to account for van der Waals dispersion corrections.[42] Slab models of 6-atomic-layer $NiFe_2O_4$(400), 4-atomic-layer Ti_2C_3(002), and 2-layer graphite surfaces with a vacuum of 15 Å were used for the calculations. Brillouin zone sampling was set to 3 × 3 × 1, 3 × 3 × 1, and the Γ point, respectively, for the $NiFe_2O_4$(400), Ti_2C_3(002), and graphite surfaces. The calculations were considered converged when the maximum forces on unconstrained atoms were less than 0.05 eV $Å^{-1}$. During calculations, only atoms at the top two layers were allowed to fully relax, while the others were fixed to their bulk positions (except for the graphite case, in which all atoms were allowed to fully relax). The H-atom adsorption energy can be calculated using $E_{ads} = E_{(slab+H)} - E_{(slab)} - 1/2E_{(H2)}$, corresponding to the total energies of the H-atom adsorbed on the slab surface, clean slab surface, and isolated H_2 molecules, respectively. On the basis of this definition, a negative E_{ads} indicates that the adsorption is exothermic.

Results and discussion

Characterization of the electrodes

In this work, nanocasting using SBA-15 as the hard template was employed to introduce the porosity feature in the as-prepared *m*-$NiFe_2O_4$. Fig. 1a presents the results obtained from XRD analysis. Based on the results, the reaction product collected from the nanocasting could unambiguously be ascribed as the spinel $NiFe_2O_4$. This is proven by the similarity of the observed Bragg's diffraction pattern to the standard (JCPDS 74-2081 for crystal plane of spinel $NiFe_2O_4$) and those reported in the literature.[24,43,44] Here, the results also revealed that no sign of the characteristic broad peak for amorphous

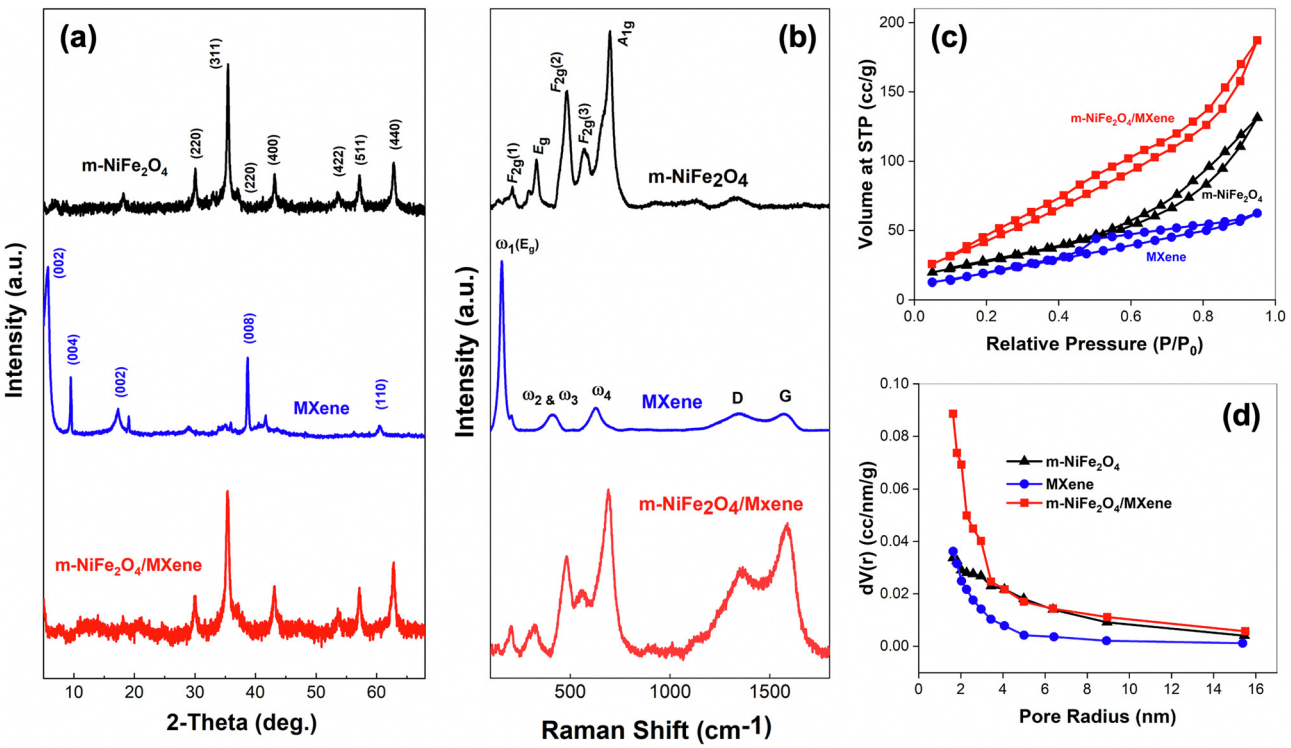

Fig. 1 (a) XRD patterns, (b) Raman spectra, (c) N_2 adsorption–desorption isotherms, and (d) pore size distribution plots of *m*-$NiFe_2O_4$, MXene, and *m*-$NiFe_2O_4$/Mxene composite.

silica at low diffraction angle was observed, suggesting that the removal of the SBA-15 template was successful (see Fig. S1a, ESI† for the XRD pattern of the as-prepared SBA-15). Furthermore, the XRD analysis results also suggested that the etching and exfoliation method successfully converted Ti_3AlC_2 into $Ti_3C_2T_x$ MXene. As shown in Fig. 1a, the formation of a $Ti_3C_2T_x$ MXene phase is signified by a shift of a sharp peak at a low diffraction angle of 9.33° corresponding to the (002) plane of Ti_3AlC_2 to a lower angle of 5.72° due to the etching of the Al layer by HF (Fig. S1b, ESI†).[45–47] Additionally, it is also reported that the shift of such a (002) peak can be associated with the increase of d-spacing and c-lattice parameters due to the formation of $Ti_3C_2T_x$ MXene from the etched Ti_3AlC_2.[48] Finally, the results also demonstrated that a nanocomposite of the as-prepared *m*-$NiFe_2O_4$ and MXene was successfully prepared using the hydrothermal method (Fig. 1a). This is indicated by the appearance of characteristic Bragg's peaks for both materials in the diffraction pattern of the composite.

Furthermore, Fig. 1b shows the Raman spectra of *m*-$NiFe_2O_4$, MXene, and the *m*-$NiFe_2O_4$/MXene composite. Based on the results, it is evident that the observation from XRD analysis was also in agreement with the results of spectroscopic analysis. Here, the Raman scattering spectrum of *m*-$NiFe_2O_4$ exhibited the characteristic vibration modes of $F_{2g}(1)$, E_g, $F_{2g}(2)$, $F_{2g}(3)$, and A_{1g} for the spinel structure of $NiFe_2O_4$, which were also observed elsewhere.[49,50] Meanwhile, several characteristic vibration modes for MXene were also observed and matched well with those reported in the literature.[51–53] In general, vibration modes of $Ti_3C_2T_x$ MXene can be divided into four regions, *i.e.*, (i) the resonant peak, (ii) A_{1g} (out-of-plane) vibrations for Ti, C, and O atoms, (iii) the vibration of the surface group, and (iv) the region for carbon vibrations.[53] According to the results, it is evident that the Raman spectra of Mxene exhibited a characteristic peak at 155 cm^{-1}, which could be assigned to the doubly degenerated ω_1 (E_g) mode for the in-plane surface Ti and C atom vibrations (Fig. 1b). Additionally, the disappearance of the ω_1 peak at 252 cm^{-1} and a significant decrease in the peak intensities of ω_2 and ω_3 (433 cm^{-1}) and ω_4 (613 cm^{-1}) from Ti_3AlC_2 indicates that the successfulness of the Al etching process (Fig. S1c, ESI†).[51] Finally, Raman spectroscopy also provided the supporting evidence for the formation of the *m*-$NiFe_2O_4$/MXene composite. As shown in Fig. 1b, the spectrum of the *m*-$NiFe_2O_4$/MXene composite was indeed a combination of both the spectra of *m*-$NiFe_2O_4$ and MXene.

In addition, Brunauer–Emmett–Teller (BET) and Barret–Joyner–Halenda (BJH) analyses were also carried out to study the surface properties of the electrocatalysts. As shown in Fig. 1c, it is evident that the as-prepared *m*-$NiFe_2O_4$ exhibited the desired mesoporous features because of nanocasting using SBA-15 as the hard template. Based on the results, N_2 adsorption–desorption isotherms clearly revealed that *m*-$NiFe_2O_4$ exhibited a typical IUPAC's type IV isotherm. A similar feature was also observed for the mesoporous silica SBA-15 template (see Fig. S2a, ESI†). This suggests that the nanocasting approach was able to preserve the mesoporosity features of the SBA-15 template after its removal, making the resulting *m*-$NiFe_2O_4$ had the same mesoporosity features with a large BET surface area of 102.4 m^2 g^{-1}. A similar observation was also reported elsewhere.[24] Nevertheless, it is worth noting that the as-prepared *m*-$NiFe_2O_4$ seems to have a more complex network porous system than that of the SBA-15 template. This is indicated by the fact that *m*-$NiFe_2O_4$ exhibited the H3 hysteresis loop as opposed to the H1 hysteresis loop of SBA-15 (Fig. S2b, ESI†). Additionally, BJH pore size estimation also revealed that *m*-$NiFe_2O_4$ had a smaller pore size and volume than SBA-15 (Fig. 1d and Table 1). Moreover, the results also demonstrated that the surface properties of MXene and the corresponding *m*-$NiFe_2O_4$/MXene composite follow the type IV isotherm with the H3 hysteresis loop, suggesting the similar mesoporosity features with large surface areas (Fig. 1c). However, it is interesting to note that the estimated *m*-$NiFe_2O_4$/MXene nanocomposite's surface area was found to be total areas of both *m*-$NiFe_2O_4$ and MXene (Table 1). This suggests that the integration of the two materials did not alter their individual porosity.

Table 1 Surface properties of mesoporous silica SBA-15 and the as-prepared electrocatalysts

Entry	BET surface area (m^2 g^{-1})	BJH pore size (nm)	BJH pore volume (cm^3 g^{-1})
SBA-15	557.1	5.162	0.611
m-$NiFe_2O_4$	102.4	3.268	0.117
MXene	77.9	3.268	0.076
m-$NiFe_2O_4$/MXene	176.7	3.267	0.256

Structural and morphological analysis

Further investigation using electron microscopy was also carried out to study the structural and morphological features of the electrocatalysts. Fig. 2 presents the micrographic images of the samples obtained from both TEM and SEM analyses. Based on the results, it is evident that the as-prepared *m*-$NiFe_2O_4$ exhibited the desired parallel interconnected nanowire structure as a result of the nanocasting method using SBA-15 as the hard template (Fig. 2a). It is believed that such a unique structural morphology was originated from the ability of Fe^{3+} and Ni^{2+} ion precursors to penetrate and transform into the corresponding $NiFe_2O_4$ inside the pores and channels of SBA-15. This is true since mesoporous silica SBA-15 consists of the typical highly ordered three dimensional parallel interconnected hexagonal pores and channels (Fig. S3, ESI†). As a result, the resulting $NiFe_2O_4$ would pertain to the negative structural copy of SBA-15 after its removal. This is proven by the similarity between the diameter of *m*-$NiFe_2O_4$ nanowires ($\sim 5.64 \pm 0.18$ nm) and the pore diameter of SBA-15 ($\sim 5.66 \pm 0.27$ nm). Moreover, such a porosity feature of the as-prepared *m*-$NiFe_2O_4$ was also supported by the results obtained from SEM analysis (Fig. 2d). As shown, the interconnected nanowires tend to clump together and form larger irregular clusters, making the additional porosity features in the bulk. Finally, further analysis using SAED also provided the supporting evidence for the formation of a highly crystalline spinel structure of $NiFe_2O_4$ due to the appearance of the characteristic ring patterns similar to those reported in the database and the literature.[16,43,54]

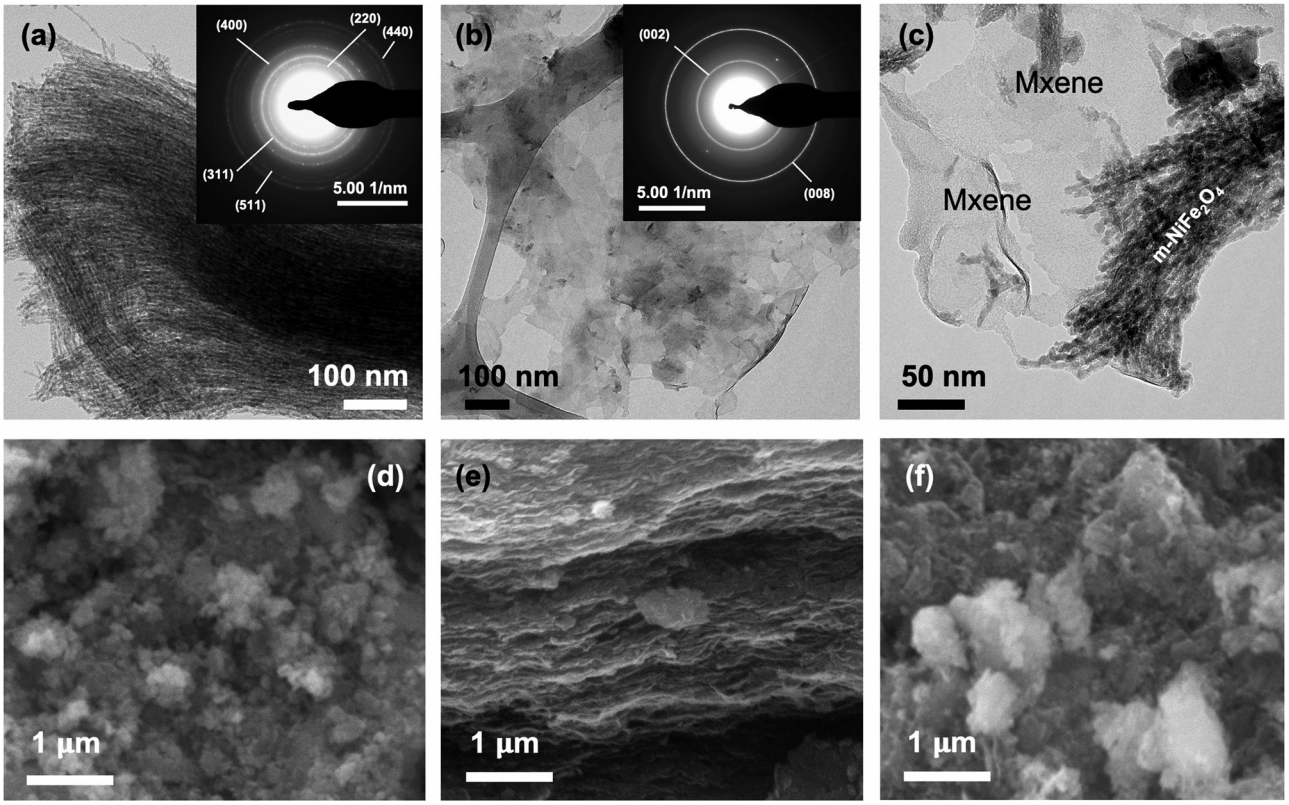

Fig. 2 (a–c) TEM images (insets: SAED analyses) and (d–f) SEM images of *m*-$NiFe_2O_4$, MXene, and *m*-$NiFe_2O_4$/Mxene composite, respectively.

On the other hand, TEM analysis revealed that the as-prepared MXene exhibited a sheet-like morphology (Fig. 2b). This is expected since etching, dealumination, and exfoliation of Ti_3AlC_2 would result in the formation of few layers of MXene flakes, which was also reported in other publications elsewhere.[55,56] Besides, the formation of a $Ti_3C_2T_x$ MXene phase was also supported by the obtained ring patterns from SAED analysis (Fig. 2b inset). Furthermore, such a unique structural feature was also supported by the cross-sectional SEM images of the as-prepared MXene (Fig. 2e). Based on the results, it is evident that the morphological structure of MXene indeed resembles stacking layers of MXene sheet flakes. Finally, both TEM and SEM images also confirmed the formation of *m*-$NiFe_2O_4$/MXene composites (Fig. 2c and 2f). As shown, the results demonstrated that both *m*-$NiFe_2O_4$ and MXene indeed coexisted after their integration during the hydrothermal treatment (see Fig. S4, ESI† for the EDS analysis of the composite).

Electrochemical activity

In this study, the performance of electrocatalysts in the HER was evaluated and compared with a Pt wire in 1 M NaOH. Fig. 3a shows the polarization curves of the electrocatalysts obtained from LSV analysis. Based on the results, it is evident that the catalytic activity of the nanocomposite was found to be superior to that of MXene or *m*-$NiFe_2O_4$, suggesting the synergistic effect between the two materials in facilitating the HER. This is proven by the comparative values of both onset and overpotentials of the as-prepared electrocatalysts, even though they were still inferior to those of the Pt wire (Table 2). Based on the results, it is evident that *m*-$NiFe_2O_4$/MXene exhibited a much lower onset potential (440 mV) than those of pristine MXene (510 mV) and *m*-$NiFe_2O_4$ (486 mV) at a considerably very low catalyst mass loading on GCE supports. Furthermore, the overpotential at a cathodic current of 10 mA cm^{-2} (η_{10}) for *m*-$NiFe_2O_4$/MXene was also found to be more positive (584 mV) as compared to those of pristine MXene (650 mV) and *m*-$NiFe_2O_4$ (788 mV). Such an improvement in catalytic activity was expected mainly due to the synergistic effect of the high surface area of *m*-$NiFe_2O_4$ and the high conductivity feature of MXene. Nevertheless, it is also worth noting that *m*-$NiFe_2O_4$ showed a better catalytic activity in the HER than MXene. It is believed that such a phenomenon was primarily caused by the high surface area due to the mesoporous feature of *m*-$NiFe_2O_4$ (Table 1). Consequently, more active sites can be developed that facilitate the HER.

According to the literature, it is reported that the reaction mechanism of water electrolysis is largely influenced by the pH of an electrolyte.[57] In general, the HER under alkaline conditions is kinetically and thermodynamically harder than that under acidic conditions. This is primarily due to the requirement of extra energy to produce protons from water molecules.[58,59] Various studies have suggested that the HER under alkaline conditions could proceed *via* either Volmer–Heyrovsky or Volmer–Tafel pathways.[60] Typically, the reaction is initiated by the electrochemical hydrogen adsorption at the

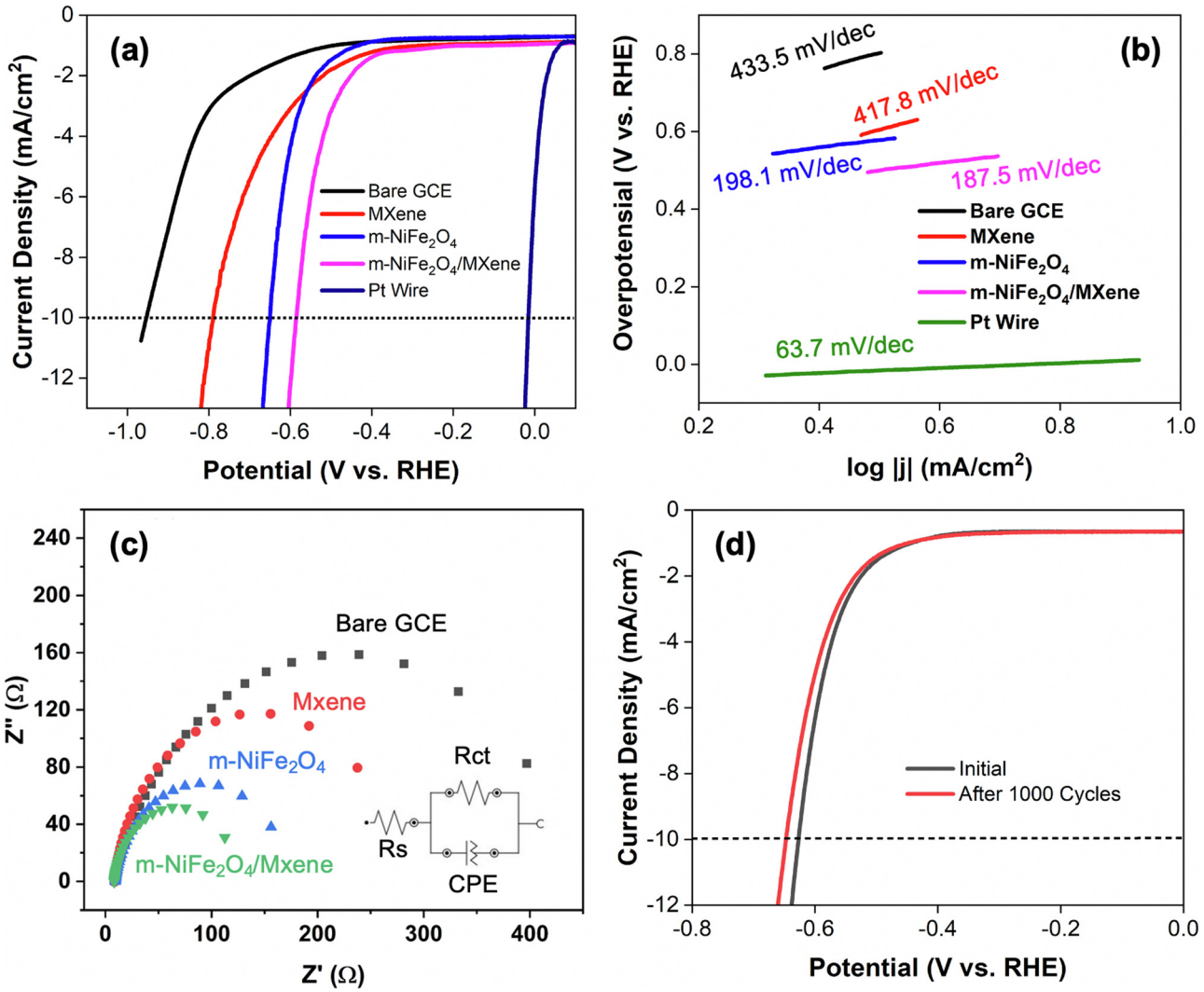

Fig. 3 (a) Polarization curves of bare GCE, MXene, *m*-$NiFe_2O_4$, *m*-$NiFe_2O_4$/Mxene, and Pt Wire at 1M NaOH, (b) the corresponding Tafel plots, (c) and Nyquist plots obtained from the electrochemical impedance spectroscopy (EIS) analysis and (d) polarization curves of *m*-$NiFe_2O_4$/Mxene before and after 1000 cycles.

Table 2 Electrochemical activities of various electrocatalysts for the HER in 1 M NaOH

Electrocatalyst	Onset potential (mV *vs.* RHE)	Overpotential[a] (mV *vs.* RHE)	Tafel slope (mV dec^{-1})
GCE	756	952	433.5
MXene	510	788	417.8
m-$NiFe_2O_4$	486	650	198.1
m-$NiFe_2O_4$/MXene	440	584	187.5
Pt wire	2	14	63.7

[a] At 10 mA cm^{-2}.

surface of the catalyst (Volmer reaction), which can be expressed as follows:[61]

$$H_2O + M + e^- \rightleftharpoons M - H^* + OH^- \text{ (Volmer)} \quad (2)$$

Subsequently, the reaction could proceed to either electrochemical desorption step (Heyrovsky reaction) or chemical desorption step (Tafel reaction) depending upon the nature of the catalyst, which can be expressed as follows:

$$H_2O + e^- + M - H^* \rightleftharpoons H_2 + OH^- + M \text{ (Heyrovsky)} \quad (3)$$

$$2M - H^* \rightleftharpoons H_2 + 2M \text{ (Tafel)} \quad (4)$$

Typically, Tafel analysis is used to determine the reaction mechanism and kinetics.[60,61] By estimating the value of the Tafel slope obtained from plotting the overpotential as a function of log|*j*|, one could simply estimate the performance of a catalyst and its possible reaction mechanism. In general, a small Tafel slope is preferred since it implies a better and faster electron-transfer kinetics.[61] Fig. 3b shows the corresponding Tafel plots for the electrocatalysts in 1 M NaOH. Based on the results, it is evident that *m*-$NiFe_2O_4$/MXene was obtained as the most active electrocatalyst after the Pt wire. This is proven by its low Tafel slope (187.5 mV dec^{-1}) comparatively than those of pristine *m*-$NiFe_2O_4$ and MXene (Table 2). Such a low Tafel slope

Table 3 HER performance of several developed materials using MXene and $NiFe_2O_4$

Electrocatalyst	Electrolyte	Overpotential (mV *vs.* RHE)[a]	Tafel slope (mV dec^{-1})	Ref.
B-$Ti_3C_2T_x$	0.5 M H_2SO_4	504	288.0	62
Ru@$Ti_3C_2T_x$	0.5 M H_2SO_4	241	158.0	63
$Ti_3C_2T_x$	0.5 M H_2SO_4	>800	147.0	64
MoS_2/$Ti_3C_2T_x$	0.5 M H_2SO_4	>400	68.0	63
MXene/NF	1 M KOH	>300	164.0	64
$NiFe_2O_4$@N/C-800	1 M KOH	>300	133.8	65
m-$NiFe_2O_4$/MXene	1 M KOH	584	187.5	This work

[a] At 10 mA cm^{-2}.

suggests that the integration of the two materials was able to synergistically enhance reaction kinetics, which led to the improvement of HER performance. The results from Tafel analysis also revealed that the reaction mechanism for all the catalysts follows the Volmer–Heyrovsky route, where the desorption step was believed to be the rate determining step.

In addition, Nyquist plots from EIS analysis also revealed that charge transfer resistance (Rct) of the *m*-$NiFe_2O_4$/MXene composite was found to be the smallest among the as-prepared electrocatalysts (Fig. 3c). Based on the estimation, the values of R_{ct} of bare GCE, pristine Mxene and *m*-$NiFe_2O_4$, and the corresponding value of *m*-$NiFe_2O_4$/MXene were found to be 479.6, 171.5, 257.5, and 127.7 Ω, respectively. This suggests that the integration of *m*-$NiFe_2O_4$ and MXene is responsible for the enhancement of conductivity of the material and it thus improves its catalytic activity. However, it is worth noting that the major contribution for such conductivity enhancement most likely comes from MXene due to its high conductivity. Moreover, the results from the stability test also demonstrated that the performance of *m*-$NiFe_2O_4$/MXene in the HER was found to be very stable, even after 1000 cycles (Fig. 3d). Additionally, the performance of *m*-$NiFe_2O_4$/MXene in the HER was also found to be comparable with those reported elsewhere (Table 3).

To obtain further insight into the different electrocatalytic performances, we have performed a set of DFT calculations in which the H atom is adsorbed on the surface of several planes (Fig. 4). The calculated energies are tabulated in Table 4. As seen, the H atom positioned on the top of the graphite surface has a positive value (1.49 eV). Contrarily, the H atom is exothermically adsorbed on the surface of Ti_3C_2 (MXene) and $NiFe_2O_4$, indicating the H atom stabilization. These results

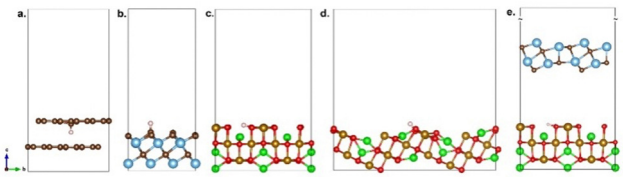

Fig. 4 Optimized structures of H-atom adsorption on (a) graphite, (b) Ti_2C_3 (002), (c) $NiFe_2O_4$ (400), (d) $NiFe_2O_4$ (311), and (e) $NiFe_2O_4$(400)/Ti_2C_3(002) (color designation: light brown: carbon; red: oxygen; white: hydrogen; light blue: titanium; green: nickel; and brown: iron).

Table 4 Adsorption energy of hydrogen atoms on each studied electrocatalyst

Electrocatalyst	H-atom position	E_{ads} (eV)
Graphite	Top	1.49
Ti_3C_2 (002)	Top of C atom	−2.41
$NiFe_2O_4$ (400)	Top of O atom	−6.53
$NiFe_2O_4$ (311)	Top of O atom	−1.64
$NiFe_2O_4$(400)/Ti_2C_3(002)	Top of O atom	−10.55

explain the better HER performance over Ti_3C_2 and $NiFe_2O_4$ than bare glassy carbon. Moreover, the adsorption energies of the H atom on the (400) and (311) planes are −6.53 eV and −1.64 eV, respectively. The former is more exothermic, while the latter is less exothermic than that on Ti_3C_2. Note that $NiFe_2O_4$ has a better electrocatalytic performance compared to Ti_3C_2. Hence, the H atom is preferably adsorbed on $NiFe_2O_4$ (400) plane. Ultimately, the H atom located at the interface between $NiFe_2O_4$ (400) and Ti_2C_3(002) planes shows the most exothermic adsorption; thus, the most stabilized H atom. The trend is in line with those in the overpotential and Tafel slopes. This insight could be utilized to further enhance the performance of $NiFe_2O_4$-based electrocatalysts through crystal face engineering.

Conclusions

In conclusion, we have successfully synthesized and characterized a mesoporous $NiFe_2O_4$/MXene nanocomposite using SBA-15 as a template for the alkaline hydrogen evolution reaction (HER). The nanocasting method using SBA-15 as a template allowed the as-prepared $NiFe_2O_4$ to possess a large surface area of 102.4 m^2 g^{-1}, providing abundant active sites for the HER process. The electrochemical measurements revealed that the $NiFe_2O_4$/MXene nanocomposite exhibited a synergistic effect in facilitating the HER, as evidenced by a low onset overpotential of –440 mV and a small Tafel slope of 187.5 mV per decade. The nanocomposite also demonstrated excellent long-term stability for the HER in alkaline electrolytes. However, it is important to note that the results from density functional theory (DFT) calculations revealed that H atoms were preferred to be absorbed on the surface of $NiFe_2O_4$ rather than MXene. This suggests that $NiFe_2O_4$ played a more dominant role in the HER catalytic process within the nanocomposite. Nevertheless, the incorporation of MXene as a conductive additive and the unique mesoporous structure derived from the SBA-15 template still contributed to the enhanced electrocatalytic activity of the nanocomposite.

Conflicts of interest

There are no conflicts to declare.

Acknowledgements

The authors would like to acknowledge the financial support provided by the Directorate of Research and Development,

Universitas Indonesia under Hibah PUTI Q1 2023 (Contract No. NKB-483/UN2.RST/HKP.05.00/2023).

References

1 M. Khalil, J. Gunlazuardi, T. A. Ivandini and A. Umar, Photocatalytic conversion of CO_2 using earth-abundant catalysts: A review on mechanism and catalytic performance, *Renewable Sustainable Energy Rev.*, 2019, **113**, 109246.
2 G. Zhao, K. Rui, S. X. Dou and W. Sun, Heterostructures for electrochemical hydrogen evolution reaction: a review, *Adv. Funct. Mater.*, 2018, **28**, 1803291.
3 H. B. Gray, Powering the planet with solar fuel, *Nat. Chem.*, 2009, **1**, 7.
4 A. Kudo and Y. Miseki, Heterogeneous photocatalyst materials for water splitting, *Chem. Soc. Rev.*, 2009, **38**, 253–278.
5 N. S. Lewis and D. G. Nocera, Powering the planet: Chemical challenges in solar energy utilization, *Proc. Natl. Acad. Sci. U. S. A.*, 2006, **103**, 15729–15735.
6 Z. Su, Q. Huang, Q. Guo, S. J. Hoseini, F. Zheng and W. Chen, Metal–organic framework and carbon hybrid nanostructures: Fabrication strategies and electrocatalytic application for the water splitting and oxygen reduction reaction, *Nano Res. Energy*, 2023, DOI: **10.26599/NRE.2023.9120078**.
7 K. Zhang, *et al.*, Status and perspectives of key materials for PEM electrolyzer, *Nano Res. Energy*, 2022, **1**, e9120032.
8 I. Roger, M. A. Shipman and M. D. Symes, Earth-abundant catalysts for electrochemical and photoelectrochemical water splitting, *Nat. Rev. Chem.*, 2017, **1**, 1–13.
9 M. Gong, D.-Y. Wang, C.-C. Chen, B.-J. Hwang and H. Dai, A mini review on nickel-based electrocatalysts for alkaline hydrogen evolution reaction, *Nano Res.*, 2016, **9**, 28–46.
10 M. I. Jamesh, Y. Kuang and X. Sun, Constructing Earth-abundant 3D Nanoarrays for Efficient Overall Water Splitting–A Review, *ChemCatChem*, 2019, **11**, 1550–1575.
11 J. Wang, *et al.*, Earth-abundant transition-metal-based bifunctional catalysts for overall electrochemical water splitting: A review, *J. Alloys Compd.*, 2020, **819**, 153346.
12 X. Kong, *et al.*, Plasma-assisted synthesis of nickel-cobalt nitride–oxide hybrids for high-efficiency electrochemical hydrogen evolution, *Mater. Today Energy*, 2021, **21**, 100784.
13 J. Fournier, L. Brossard, J. Y. Tilquin, J. P. Dodelet, D. Guay and H. Ménard, Hydrogen evolution reaction in alkaline solution: Catalytic influence of Pt supported on graphite vs. Pt inclusions in graphite, *J. Electrochem. Soc.*, 1996, **143**, 919.
14 W. Sheng, H. A. Gasteiger and Y. Shao-Horn, Hydrogen oxidation and evolution reaction kinetics on platinum: acid vs alkaline electrolytes, *J. Electrochem. Soc.*, 2010, **157**, B1529.
15 H. Yang, *et al.*, Metastable-phase platinum oxide for clarifying the Pt–O active site for the hydrogen evolution reaction, *Energy Environ. Sci.*, 2023, **16**, 574–583.
16 D. Chanda, J. Hnát, M. Paidar, J. Schauer and K. Bouzek, Synthesis and characterization of $NiFe_2O_4$ electrocatalyst for the hydrogen evolution reaction in alkaline water electrolysis using different polymer binders, *J. Power Sources*, 2015, **285**, 217–226.
17 D. Chen, F. Zhang, W. Wang, Y. Yang and G. Qian, Synergistic effect of PANI and $NiFe_2O_4$ for photocatalytic hydrogen evolution under visible light, *Int. J. Hydrogen Energy*, 2018, **43**, 2121–2129.
18 L. Meng, *et al.*, Rational construction of uniform CoS/$NiFe_2O_4$ heterostructure as efficient bifunctional electrocatalysts for hydrogen evolution and oxygen evolution reactions, *Electrochim. Acta*, 2022, **404**, 139596.
19 P. Shinde, C. S. Rout, D. Late, P. K. Tyagi and M. K. Singh, Optimized performance of nickel in crystal-layered arrangement of NiFe2O4/rGO hybrid for high-performance oxygen evolution reaction, *Int. J. Hydrogen Energy*, 2021, **46**, 2617–2629.
20 R. Nivetha, S. Chella, P. Kollu, S. K. Jeong, A. Bhatnagar and N. G. Andrews, Cobalt and nickel ferrites based graphene nanocomposites for electrochemical hydrogen evolution, *J. Magn. Magn. Mater.*, 2018, **448**, 165–171.
21 A. Mukherjee, S. Chakrabarty, W.-N. Su and S. Basu, Nanostructured nickel ferrite embedded in reduced graphene oxide for electrocatalytic hydrogen evolution reaction, *Mater. Today Energy*, 2018, **8**, 118–124.
22 A. H. Lu and F. Schüth, Nanocasting: a versatile strategy for creating nanostructured porous materials, *Adv. Mater.*, 2006, **18**, 1793–1805.
23 D. Erika, S. Mardiana, C. B. Rasrendra, M. Khalil and G. T. M. Kadja, Nanocasting nanoporous nickel oxides from mesoporous silicas and their comparative catalytic applications for the reduction of p-nitrophenol, *Chem. Phys. Lett.*, 2022, **803**, 139809.
24 E. Kamali-Heidari and A. Kamyabi-Gol, Synthesis of mesoporous nickel iron oxide as a new anode material for high performance lithium ion batteries, *Phys. B*, 2019, **570**, 176–181.
25 Z. Kang, *et al.*, Recent progress of MXenes and MXene-based nanomaterials for the electrocatalytic hydrogen evolution reaction, *J. Mater. Chem. A*, 2021, **9**, 6089–6108.
26 M. Zubair, M. M. U. Hassan, M. T. Mehran, M. M. Baig, S. Hussain and F. Shahzad, 2D MXenes and their heterostructures for HER, OER and overall water splitting: a review, *Int. J. Hydrogen Energy*, 2021, DOI: **10.1016/j.ijhydene.2021.10.248**.
27 F. Sagita, C. L. Radiman, M. Ledyastuti, M. Khalil and G. T. M. Kadja, Salt-modified MXene membrane for ultrafast and efficient cationic and anionic dyes removal, *J. Water Process Eng.*, 2022, **49**, 103133.
28 Y. Sun, *et al.*, Eosin Y-sensitized partially oxidized Ti_3C_2 MXene for photocatalytic hydrogen evolution, *Catal. Sci. Technol.*, 2019, **9**, 310–315.
29 P. K. Jiwanti, A. M. Alfaza, G. T. M. Kadja, M. Khalil and Y. Einaga, Electrochemical study of CO2 reduction on $Ti_3C_2T_x$ modified boron-doped diamond electrode, *Inorg. Chem. Commun.*, 2022, **137**, 109228.
30 X. Zhang, *et al.*, Platinum Nanoparticle-Deposited $Ti_3C_2T_x$ MXene for Hydrogen Evolution Reaction, *Ind. Eng. Chem. Res.*, 2020, **59**, 1822–1828.

31 Z. Lv, M. Wang, D. Liu, K. Jian, R. Zhang and J. Dang, Synergetic Effect of Ni2P and MXene Enhances Catalytic Activity in the Hydrogen Evolution Reaction, *Inorg. Chem.*, 2021, **60**, 1604–1611.
32 D. Zhao, *et al.*, Triblock Copolymer Syntheses of Mesoporous Silica with Periodic 50 to 300 Angstrom Pores, *Science*, 1998, **279**, 548–552.
33 P. Hohenberg and W. Kohn, Inhomogeneous electron gas, *Phys. Rev.*, 1964, **136**, B864.
34 W. Kohn and L. J. Sham, Self-consistent equations including exchange and correlation effects, *Phys. Rev.*, 1965, **140**, A1133.
35 G. Kresse and J. Furthmüller, Efficiency of ab-initio total energy calculations for metals and semiconductors using a plane-wave basis set, *Comput. Mater. Sci.*, 1996, **6**, 15–50.
36 G. Kresse and J. Furthmüller, Efficient iterative schemes for ab initio total-energy calculations using a plane-wave basis set, *Phys. Rev. B: Condens. Matter Mater. Phys.*, 1996, **54**, 11169.
37 P. E. Blöchl, Projector augmented-wave method, *Phys. Rev. B: Condens. Matter Mater. Phys.*, 1994, **50**, 17953.
38 G. Kresse and D. Joubert, From ultrasoft pseudopotentials to the projector augmented-wave method, *Phys. Rev. B: Condens. Matter Mater. Phys.*, 1999, **59**, 1758.
39 J. P. Perdew, K. Burke and M. Ernzerhof, Generalized gradient approximation made simple, *Phys. Rev. Lett.*, 1996, **77**, 3865.
40 S. L. Dudarev, G. A. Botton, S. Y. Savrasov, C. Humphreys and A. P. Sutton, Electron-energy-loss spectra and the structural stability of nickel oxide: An LSDA+ U study, *Phys. Rev. B: Condens. Matter Mater. Phys.*, 1998, **57**, 1505.
41 L. Wang, T. Maxisch and G. Ceder, Oxidation energies of transition metal oxides within the GGA+ U framework, *Phys. Rev. B: Condens. Matter Mater. Phys.*, 2006, **73**, 195107.
42 S. Grimme, Semiempirical GGA-type density functional constructed with a long-range dispersion correction, *J. Comput. Chem.*, 2006, **27**, 1787–1799.
43 Y. Guo, *et al.*, Electrostatic self-assembled $NiFe_2O_4/Ti_3C_2T_x$ MXene nanocomposites for efficient electromagnetic wave absorption at ultralow loading level, *Adv. Compos. Hybrid Mater.*, 2021, **4**, 602–613.
44 E. K. Heidari, B. Zhang, M. H. Sohi, A. Ataie and J.-K. Kim, Sandwich-structured graphene–$NiFe_2O_4$–carbon nanocomposite anodes with exceptional electrochemical performance for Li ion batteries, *J. Mater. Chem. A*, 2014, **2**, 8314–8322.
45 W. Feng, *et al.*, Ti_3C_2 MXene: a promising microwave absorbing material, *RSC Adv.*, 2018, **8**, 2398–2403.
46 M. Naguib, *et al.*, Two-dimensional nanocrystals produced by exfoliation of Ti_3AlC_2, *Adv. Mater.*, 2011, **23**, 4248–4253.
47 L. Yao, X. Tian, X. Cui, R. Zhao, X. Xiao and Y. Wang, Partially oxidized $Ti_3C_2T_x$ MXene-sensitive material-based ammonia gas sensor with high-sensing performances for room temperature application, *J. Mater. Sci.: Mater. Electron.*, 2021, **32**, 27837–27848.
48 M. Naguib, V. N. Mochalin, M. W. Barsoum and Y. Gogotsi, 25th anniversary article: MXenes: a new family of two-dimensional materials, *Adv. Mater.*, 2014, **26**, 992–1005.
49 A. Ahlawat and V. Sathe, Raman study of $NiFe_2O_4$ nanoparticles, bulk and films: effect of laser power, *J. Raman Spectrosc.*, 2011, **42**, 1087–1094.
50 P. Sahoo, R. G. Shrestha, L. K. Shrestha, J. P. Hill, T. Takei and K. Ariga, Surface oxidized carbon nanotubes uniformly coated with nickel ferrite nanoparticles, *J. Inorg. Organomet. Polym. Mater.*, 2016, **26**, 1301–1308.
51 A. Iqbal and N. M. Hamdan, Investigation and Optimization of Mxene Functionalized Mesoporous Titania Films as Efficient Photoelectrodes, *Materials*, 2021, **14**, 6292.
52 S. Nam, S. Umrao, S. Oh, K. H. Shin, H. S. Park and I.-K. Oh, Sonochemical self-growth of functionalized titanium carbide nanorods on Ti_3C_2 nanosheets for high capacity anode for lithium-ion batteries, *Composites, Part B*, 2020, **181**, 107583.
53 A. Sarycheva and Y. Gogotsi, Raman spectroscopy analysis of the structure and surface chemistry of $Ti_3C_2T_x$ MXene, *Chem. Mater.*, 2020, **32**, 3480–3488.
54 S. Iraqui, S. S. Kashyap and M. H. Rashid, $NiFe_2O_4$ nanoparticles: an efficient and reusable catalyst for the selective oxidation of benzyl alcohol to benzaldehyde under mild conditions, *Nanoscale Adv.*, 2020, **2**, 5790–5802.
55 G. Cui, L. Wang, L. Li, W. Xie and G. Gu, Synthesis of CuS nanoparticles decorated $Ti_3C_2T_x$ MXene with enhanced microwave absorption performance, *Prog. Nat. Sci.: Mater. Int.*, 2020, **30**, 343–351.
56 E. Satheeshkumar, T. Makaryan, A. Melikyan, H. Minassian, Y. Gogotsi and M. Yoshimura, One-step solution processing of Ag, Au and Pd@ MXene hybrids for SERS, *Sci. Rep.*, 2016, **6**, 1–9.
57 N. Mahmood, Y. Yao, J. W. Zhang, L. Pan, X. Zhang and J. J. Zou, Electrocatalysts for hydrogen evolution in alkaline electrolytes: mechanisms, challenges, and prospective solutions, *Adv. Sci.*, 2018, **5**, 1700464.
58 N. Danilovic, *et al.*, Enhancing the alkaline hydrogen evolution reaction activity through the bifunctionality of $Ni(OH)_2$/metal catalysts, *Angew. Chem.*, 2012, **124**, 12663–12666.
59 R. Subbaraman, *et al.*, Enhancing hydrogen evolution activity in water splitting by tailoring Li + -Ni $(OH)_2$-Pt interfaces, *Science*, 2011, **334**, 1256–1260.
60 J. Ding, *et al.*, Advances in the Electrocatalytic Hydrogen Evolution Reaction by Metal Nanoclusters-based Materials, *Small*, 2022, 2204524.
61 J. Zhu, L. Hu, P. Zhao, L. Y. S. Lee and K.-Y. Wong, Recent advances in electrocatalytic hydrogen evolution using nanoparticles, *Chem. Rev.*, 2019, **120**, 851–918.
62 M. Bat-Erdene, *et al.*, Highly dispersed Ru nanoparticles on boron-doped $Ti_3C_2T_x$ (MXene) nanosheets for synergistic enhancement of electrocatalytic hydrogen evolution, *Small*, 2021, **17**, 2102218.
63 L. Huang, L. Ai, M. Wang, J. Jiang and S. Wang, Hierarchical MoS_2 nanosheets integrated Ti_3C_2 MXenes for electrocatalytic hydrogen evolution, *Int. J. Hydrogen Energy*, 2019, **44**, 965–976.
64 M. Yu, Z. Wang, J. Liu, F. Sun, P. Yang and J. Qiu, A hierarchically porous and hydrophilic 3D nickel–iron/MXene electrode for accelerating oxygen and hydrogen evolution at high current densities, *Nano Energy*, 2019, **63**, 103880.
65 L. Cao, Z. Li, K. Su, M. Zhang and B. Cheng, Rational design of hollow oxygen deficiency-enriched $NiFe_2O_4$@N/rGO as bifunctional electrocatalysts for overall water splitting, *J. Energy Chem.*, 2021, **54**, 595–603.